LANGMUIR

pubs.acs.org/Langmuir Article

Tailoring Nanodiamonds for High-Contrast EPR Imaging: Size, Surface Properties, and Spectroscopic Performance

Sarah Garifo, Dimitri Stanicki, Thomas Vangijzegem, Philippe Mellet, Hugues A. Girard, Jean-Charles Arnault, Sylvie Bégin-Colin, Yves-Michel Frapart, Robert N. Muller, and Sophie Laurent*

Cite This: https://doi.org/10.1021/acs.langmuir.4c05169 Read Online

ABSTRACT: Electron paramagnetic resonance (EPR) spectroscopy is a tool that provides sensitive detection of uncoupled electron spins for a variety of applications. This technique enables the specific detection and quantification of radical species while also being able of generating high-contrast, background-free images. However, the EPR labeling and imaging techniques encounter limitations mainly due to the instability of organic radicals from organic probes, which can influence the reliability and scope of the experiment. In that context, the use of nanodiamonds (NDs) in EPR may be a promising route for understanding their unique properties and potential biomedical applications. The ability to perform EPR imaging in combination with the stable intrinsic properties of paramagnetic centers within these particles raises the possibility of extending nanodiamond-based imaging capabilities. Herein, we present a preliminary demonstration of a practical spectroscopy and imaging application using nanosized diamond particles (<18 nm) for electron paramagnetic resonance imaging (EPRI). The discretization of two different nanodiamond production sources among the most studied NDs (HPHT or detonation) allows further characterization of their physicochemical properties. In addition, we have investigated variations in the physicochemical properties of nanodiamonds, including size effects and surface treatments. Finally, we provide experimental evidence of the conditions required for optimal spectroscopic and imaging resolution (R < 1 mm) as well as achievable EPR sensitivity.

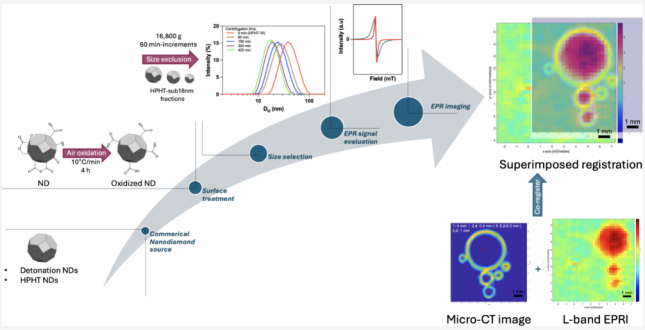

■ INTRODUCTION

Electron paramagnetic resonance (EPR), as a spectroscopic technique, is specific to the resonance of paramagnetic species such as (in)organic radicals, complexes, crystallographic defects, colored centers, or transition metal ions when subjected to a magnetic field. Many concepts in electron spin (or paramagnetic) resonance (ESR or EPR) spectroscopy are related to similar notions in nuclear magnetic resonance (NMR) spectroscopy;[1] like what NMR brings to MRI modality, EPR can enable EPR imaging (EPRI) using an additional magnetic field gradient in a set of different orientations around the sample. High-resolution images using a noninvasive imaging technique enable the specific detection and quantification of paramagnetic species with optimal resolution. The choice of the probe depends on the specific application and the physicochemical properties of the sample under study.[2] Overall, the versatility and sensitivity of EPR probes make them essential tools for a wide range of applications in medicine, industry, and the environment. The best-known probes and their applications include (i) nitroxide species for studying biological systems (i.e., superoxide spin trapping),[3,4] (ii) triarylmethyl radicals (TAMs) for oximetry (i.e., to measure oxygen concentration in biological samples for in-depth assessment of tissue oxygenation, metabolism, and redox evaluations),[5,6] and (iii) site-directed spin labeled (SDSL) nitroxides to evaluate structural and dynamic properties of organic systems, such as transmembrane transport and transcription mechanisms or as Cu(II) spin labels.[7−9] However, the stability of paramagnetic organic compounds can be influenced by a number of factors such as pH, temperature, or redox environment, influencing the reliability of the experiment. The probes, specifically tailored for paramagnetic labeling, can be assessed through EPR studies to obtain valuable information.

While we focus on the capabilities of EPR spectroscopy to analyze paramagnetic materials, particular attention is paid to nanodiamonds (NDs), whose unique properties are attracting growing interest in a variety of scientific domains. Integrating the EPR properties of NDs into the EPR imaging modality

Received: December 18, 2024
Revised: February 3, 2025
Accepted: February 5, 2025

enables in-depth characterization of these nanoplatforms, opening up new perspectives in applications ranging from nanomedicine to materials science. Indeed, nanodiamonds have emerged as promising carbon-based nanomaterials for a range of applications due to their unique advantages, particularly in the biological, medical, and imaging fields.[10−12] In these fields, the nitrogen-vacancy (NV) centers embedded in the core of the NDs are exploited for their ultrastable fluorescence properties, while some of the fluorescent probes are limited either by their photostability or cytotoxicity.[13−15] Other interests include the use of crude NDs as noncytotoxic substrates for gene and drug delivery,[11,16] as implants,[17] in tissue engineering or as powerful theranostic substrates for the targeted delivery of vaccines,[18] as chemotherapy agents,[16,19] in immunotherapeutics, as Gd- and Mn-doped (grafted) DND MRI contrast agents,[20−24] or for hyperpolarization MRI[25−28] using ND intrinsic impurities.

Apart from optical fluorescence, NMR, or hyperpolarization purposes, options for noninvasive *in vitro* and *in vivo* imaging of nanodiamonds are very limited. Three main advantages of using NDs in EPRI can be noted: The first one is closely linked to the relative stability of the radical-like paramagnetic centers (in the bulk and the core of the particle) compared with conventional organic radicals (i.e., easy reduction through metabolic pathways).[29] The second results from the nanoparticle unique characteristics; nanoparticles provide a versatile platform that can be used in a variety of biomedical and technological applications regarding their distinct physicochemical properties (enhanced surface area, properties tailoring, biocompatibility, tunable surface chemistry, and surface charge or versatility).[30] The third results from the EPR signal; the EPR signal of NDs typically exhibits a narrow line indicating well-defined electron spin states resulting in a high signal-to-noise ratio (as a function of line width). In addition, the EPR spectrum may display other specific features corresponding to (structural) defects or impurities in the diamond lattice depending on the material studied (nanodiamond source, size, surface graphitization, and crystallinity).

Two primary methods for producing nanoscale diamond particles have been introduced based on their production procedures: (i) a detonation-based synthesis where the carbon source is derived from the explosives or (ii) a mechanical grinding of high-quality HPHT (high-pressure high-temperature) diamond microcrystals into nanometric particles. Particles obtained by detonation are rather small (<10 nm) and relatively monodisperse but exhibit poor crystalline quality, whereas those obtained by fragmentation of bulk material exhibit superior crystallinity, albeit with a broader size distribution (from hundreds of micrometers to a few nanometers).[31,32] Depending on the nanodiamond synthesis procedure, their properties (size, structure, surface composition, EPR or optical luminescence properties, and crystallinity) can be significantly impacted. For example, there are many more defects in ND_{DET} compared to ND_{HPHT} as a result of the uncontrolled explosion event. These include vacancies, dislocations, domain boundaries, and amorphous carbon impurities, mainly on the surface and within the interface layer (i.e., dangling bonds).[31,32] In contrast, ND_{HPHT} defects consist of vacancies, dislocations, or stacking faults in a crystalline lattice. Furthermore, their surface properties are very different, with ND_{DET} having a complex surface with a higher density of defects, amorphous and graphitic carbons, and various functional groups, leading to aggregation due to weak electrostatic interactions.[31,32]

Ultimately, the choice between both types depends on specific requirements, such as particle size distribution, purity, surface chemistry, or fluorescence stability. In general, the small-sized detonation nanodiamond is the typical choice for MRI purposes, while larger-sized HPHT particles are suitable in tissue engineering or luminescence purpose.[33]

Here, we present the physicochemical property variations from production source, size, and surface treatments effects and EPR investigation. By means of mathematical developments, imaging optimizations, and a reliable nanodiamond strategy, we demonstrate EPRI capabilities using this nanomaterial. To our knowledge, this is the first experimental evidence of EPR imaging using NDs.

■ MATERIALS AND METHODS

Materials. The monocrystalline synthetic microdiamond powder of HPHT origin (Microdiamant MSY 0-0.03) was supplied by Pureon AG (Lengwil, Switzerland). Primary particles of the detonation nanodiamond were manufactured by NanoAmando (NanoCarbon Research Institute Ltd., Nagano, Japan). Branched poly(ethylenimine) (MW = 1200 Da, ≥99%) and ICP zirconium plasma standard were supplied by ThermoFischer Scientific (Merelbeke, Belgium). ICP multielement standard solution was supplied by Merck (Hoeilaart, Belgium). All chemicals used were of standard purity grade. Stirred cells and membranes (MWCO = 100 kDa, RC) for ultrafiltration were purchased from Metrohm (Antwerpen, Belgium).

Preparation of Nanodiamond Suspensions. Nanodiamond suspensions were prepared by dispersing diamond powders (200 mg) either used as-received ("asrec") or thermally oxidized ("ox") in deionized (DI) water. To ensure a good colloidal dispersion, particles were sonicated in DI water for 90 min (10 min steps) using an ultrasound probe (Hielscher, 200 W, 24 kHz) with an amplitude of 70% (duty cycle: 1/2) and slightly centrifuged (670*g*, 5 min) to exclude larger aggregates. Nanoparticle density was obtained gravimetrically after freeze-drying 1 mL of the suspension followed by a drying step at 80 °C for 24 h. If necessary, nanodiamonds were concentrated by a stirred ultrafiltration cell device (MWCO = 100 kDa) to reach a particle concentration of 20 mg mL^{-1}.

Oxidative Treatment by Air Annealing. A ceramic crucible filled with crude freeze-dried diamond powder was heated in a muffle furnace (heating rate: 10 °C min^{-1}) in air at 400 °C (ox-1), 450 °C (ox-2), 480 °C (ox-3), or 550 °C (ox-4) for 4 h (Nabertherm GmbH, Lilienthal, Germany) to remove the graphitic shell and modify oxidation-sensitive chemical groups. The conditions of oxidative air treatment by air annealing were studied by thermal analysis (TGA) and carried out in accordance with published procedures with some modifications.[34,35] The air-annealed (oxidized) NDs were then dispersed in DI water as previously described to obtain a gray/black nanodispersion (20 mg mL^{-1}).

Size Exclusion Process. Sub-17 nm ND_{HPHT} fractions were obtained by successive high-speed centrifugation cycles on ND_{HPHT}^{asrec} (5 mg mL^{-1}). Between each centrifugal treatment (IEC CL31R Multispeed Centrifuge, 16,800*g*; $0 < n < 7 \times 60$ min steps), the supernatant was carefully isolated, characterized, and treated again. Their notations throughout the article are written as follows: ND_{HPHT}^{1} isolated after a centrifugation cycle of 1 × 60 min; ND_{HPHT}^{2} sample isolated after 2 × 60 min, etc. This procedure was not applied to detonation nanodiamonds due to a lack of colloidal stability resulting from their aggregation state.

Physicochemical Characterization Techniques. The hydrodynamic particle size and zeta potential were determined by photon correlation spectroscopy (PCS) using a Zetasizer Nano ZS particle size analyzer (Malvern Instruments, He−Ne laser, 633 nm, scattering angle 173°) (Worcestershire, UK) on diluted suspensions (1 mg mL^{-1} in DI water, 25 °C). The refractive index of bulk diamond (2.4 at 635 nm) was used to evaluate the intensity and number-weighted

https://doi.org/10.1021/acs.langmuir.4c05169
Langmuir XXXX, XXX, XXX−XXX

distributions. PCS measurements are presented as mean values (hydrodynamic D_H^{PCS} or number diameters ($D_\#^{PCS}$) and zeta potential (ζ)) ± standard deviation. The evolution of the zeta potential was investigated in relation to pH changes; the pH of each nanodiamond sample was adjusted using diluted HNO_3 or TMAOH solution.

TEM experiments were performed with a Fei Tecnai 10 electron microscope (Oregon, USA) operating at an accelerating voltage of 80 kV under a vacuum to obtain detailed information on the morphology and the size distribution of a sample. Each specimen was prepared following a procedure slightly adapted from Rehor and Cigler.[36] Briefly, 300 mesh carbon-coated Formvar grids (Ted Pella Inc., California, USA) were pretreated using an UV/ozonizing chamber (AppliTek Scientific Instruments, Nazareth, Belgium) for 15 min. A mixture droplet (4 μL) of a branched ethylenimine polymer solution (MW = 1,2 kDa, 0.1 mg mL^{-1}) and a 0.1 mg mL^{-1} colloidal suspension was then placed on the grid, allowing the liquid to dry in air at room temperature. The statistical particle size distribution was obtained by examining multiple images of each sample using the iTEM software (Münster, Germany) using the Feret diameter as the size expression due to the irregular shape of the studied ND_{HPHT} particle. By measuring the diameter size of 400 to 500 counted particles for each sample, the mean equivalent median diameter (D^{TEM}), the polydispersity index (PDI^{TEM}), and a standard deviation (SD) from the corresponding particle suspension were calculated.[37] A size histogram showing the number-weighted distribution was obtained, and the resulting histograms were fitted with a log-normal function.

Thermogravimetric analyses (TGAs) were performed on a TA Q500 device (TA Instruments, New Castle, USA). The mass loss of predried HPHT and DET samples monitored under air was over the process for thermal stability investigation. After an isotherm at 120 °C for 10 min (heating rate: 10 °C min^{-1}), the temperature was increased from 120 to 800 °C at a heating rate of 10 °C min^{-1} under air flow (25 mL min^{-1}), and the temperature was maintained for 5 min.

The Boehm titration method was evaluated on ND_{DET}^{asresc}, $ND_{DET}^{ox\text{-}1}$, and ND_{HPHT}^{asresc} nanoparticles (10 mg mL^{-1}) under conductometric detection (SI Analytics, Lab 945, Xylem) to quantify the oxygenated functional groups present on the particle surface according to a published procedure.[38]

Infrared spectra (ATR) of dried powders were recorded on a PerkinElmer FTIR Spectrum 100 spectrometer (Manchester, UK) with an average of four scans and a resolution of 4 cm^{-1}.

Raman measurements were performed on an Xplora Raman spectrometer (Horiba) under green wavelength laser excitation (532 nm, 0.79 mW) equipped with a 1800 tr/mm grating. Prior to their characterizations, samples were dispersed in DI water and dispensed onto a Si substrate by drop-casting for analysis. Spectra have been recorded with a 10 s acquisition time, repeated 10 times. To ensure the representativeness of the spectra presented here, three different areas of the samples were systematically probed.

The surface chemistry of the nanodiamond samples was characterized by X-ray photoelectron spectroscopy (XPS) using an XPS Versa Probe Phi 5000 spectrometer (Chanhassen, USA). The X-ray source was a monochromatized Al Kα line (E_b = 1486.7 eV). Measurement of the deconvoluted *C 1s* and *O 1s* orbital peak energies was carried out using a linear baseline and Gaussian line curves of variable widths.

The elemental composition of the nanodiamonds was determined by high-resolution TEM energy-dispersive X-ray spectroscopy (HRTEM-EDX) scanning with an average of three measurements for the qualitative measurements (TEM grids: Formvar/carbon supported copper grids). Prior to quantitative analysis of impurities, the as-received detonation and HPHT powders (250.0 ± 0.1 mg) were calcinated in a muffle furnace (heating rate: 10 °C min^{-1}; 650 °C for 3 h).[39] The resulting yellow/light brown residues (6.3−3.4 mg, respectively) were then quantitatively transferred into Teflon vessels for microwave acid digestion (Milestone MLS 1200 Mega, Analis, Belgium). Levels of total uncalcinated impurities of 2.52 and 1.36%$_{w/w}$ for DET and HPHT powders, respectively, were measured gravimetrically, corresponding to 95−98% of the major carbon element in NDs. The volumes of the resulting acid-treated samples were then adjusted to 25 mL using DI water. The impurity (i.e., Ag, Al, Zn, Fe, Cr, Cu, Zr, and Mn) content was quantified by inductively coupled plasma-atomic emission spectroscopy (ICP-AES) under argon plasma on a Varian Liberty Series II instrument (Varian Inc., Palo Alto, USA). Calibration curves (R^2 > 0.99) using different dilutions of an ICP multielement standard solution were constructed to ensure the proper quantification of each metallic impurity.

EPR Spectroscopy and Imaging. *EPR Spectroscopy.* X-band electron paramagnetic resonance spectroscopy was used to identify the paramagnetic contributions to the overall EPR spectrum and to obtain quantitative information about paramagnetic centers. Samples (20 mg mL^{-1} in DI water) were analyzed at room temperature on a Bruker EMX nano (Bruker, Rheinstetten, Germany). The following spectroscopic parameters were used: 343.5 mT center field, microwave frequency of ∼9.8 GHz, magnetic field modulation amplitude of 0.1 mT, and frequency of 100 kHz and presented as the derivative of the microwave absorption over the magnetic field. In the specific case of nanodiamonds, their EPR spectra typically present a single line characterized by a narrow or large resonant shape, depending on the electron spin states. Therefore, the type of (isotropic) broadening applied to a line width (lw) is referred to as lwpp (pp, peak-to-peak) to measure the horizontal distance between the maximum and the minimum of the first-derivative EPR line shape. The *g*-factor refers to the spectroscopic splitting factor, characterizing the behavior of species in a magnetic field, and is extracted from the minima in the second-derivative EPR spectra.

Spectroscopic Simulation. EPR spectra were simulated using the EasySpin software package (Matlab).[40]

Low-Frequency EPR Settings. Low microwave spectroscopic EPR data were recorded at 1 GHz (L-band) on a CW EPR E540L spectrometer (Bruker, Rheinstetten, Germany) at room temperature.

Phantom Preparation. Nanodiamond suspensions in DI water (filled with 100−200 μL at a 10 mg mL^{-1} particle density) were placed in EPR tubes (4, 1, 0.5, 0.4, and 0.3 mm quartz capillary diameter size) inserted into a 23 mm birdcage resonator mounted inside the device for phantom imaging study.

Phantom EPR Imaging Experiments. The EPR imaging was performed using the L-band spectrometer.[40] The continuous wave system was equipped with gradient coils to obtain information about the spatial distribution of free radicals in the nanodiamond samples. Spectrometer parameters were as follows: microwave power: 50 mW; field of view (FOV) diameter: 82.4 mm; sweep width: 8.24 mT; microwave frequency: 1.105 GHz; amplitude modulation: 0.2 mT; and frequency modulation: 50 kHz. Experimental resolutions were evaluated on the basis of images of quartz capillaries (0.3−4 mm diameters) filled with nanodiamond suspensions with repositioning on anatomical images obtained via X-ray microcomputed (micro-CT) tomography.

Image Reconstruction and Mathematical Procedures. EPR image reconstruction was performed using a Total Variation algorithm-based,[41] published and usable online.[42]

X-ray Microtomographs. Micro-CT imaging was performed using a 1178 X-ray computed scanner (Skyscan, Kontich, Belgium) with the following parameter setting: 65 kV, 615 μA, and pixel size 83.82932 μm. The spatial resolution of quartz capillary diameters was determined by analyzing the micro-CT images using the Skyscan software suite. The images were co-registered using GIMP.

■ RESULTS AND DISCUSSION

Physicochemical Characterization of NDs (As-Received ND_{DET} and ND_{HPHT}). For ND_{HPHT}, we used as-received (asrec) commercially available MSY 0-0.03 powders as these are the smallest monocrystalline particles reported.[43] TEM analysis revealed NDs with irregular shapes with sharp edges and a large size distribution (17 nm; PDI^{TEM}: 1.79). The particle size distributions obtained after sonication show

https://doi.org/10.1021/acs.langmuir.4c05169
Langmuir XXXX, XXX, XXX−XXX

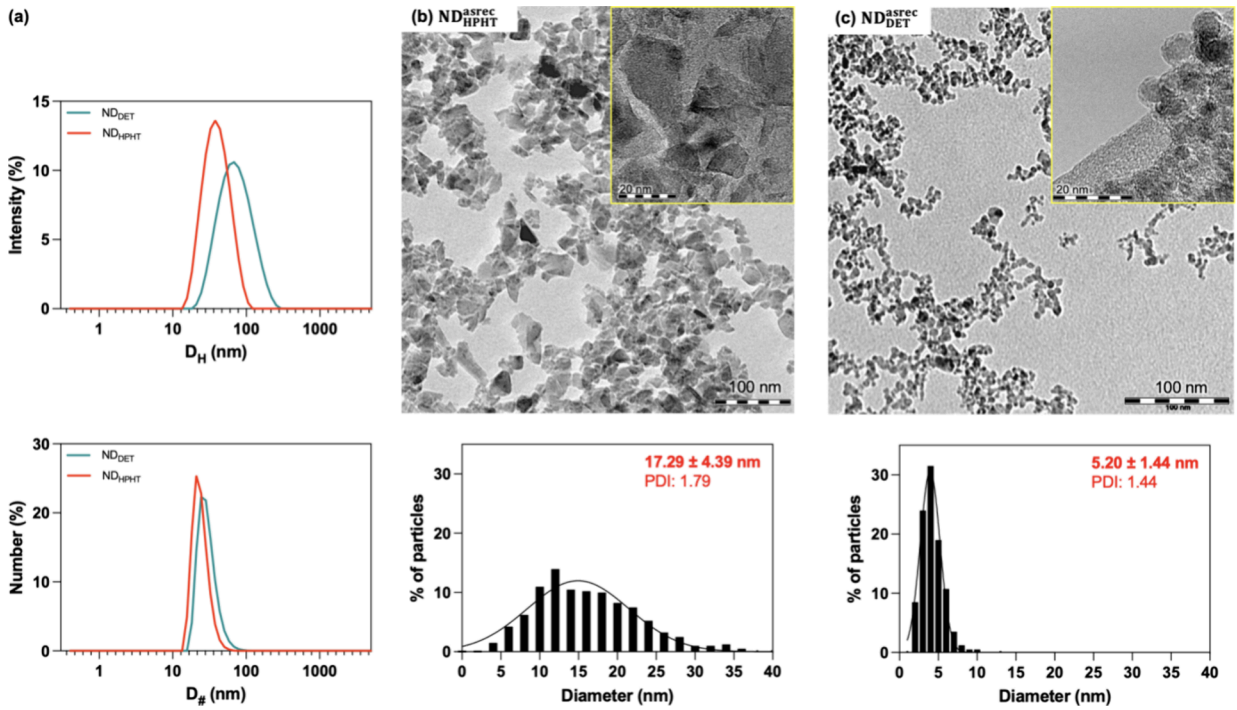

Figure 1. Size measurements. (a) Size distributions obtained by PCS (intensity-weighted (up) and number-weighted (bottom) distributions). TEM images of (b) mean 17 nm ND_{HPHT} and (c) mean 5 nm ND_{DET} (scale bars: 100 nm) and their particle size distributions. The x axis for ND_{HPHT} particle histograms is expressed as a 2 nm increment size diameter for clarity (1 nm increment size for ND_{DET}). Extensions (yellow frames) show high-resolution TEM images (scale bars: 20 nm) obtained by the HRTEM-EDX experiment (as-received HPHT and detonation samples: 200k and 250k× magnification, respectively).

narrow, almost monodisperse particle distributions (24 nm in number-weighted distributions; Figure 1a), consistent with TEM observations. For ND_{DET}, while small-sized particles were observed by TEM (5.2 nm, PDI^{TEM}: 1.44), a larger average particle size was observed using DLS (63 and 32 nm in intensity- and number-weighted distributions, respectively), suggesting the dispersion of aggregates rather than individual particles. Contrary to ND^{asrec}_{HPHT}, ND^{asrec}_{DET} was characterized by low colloidal stability (ζ = −39 and +42 mV, pH 7.3), especially when the ionic strength of the medium is increased, which could reflect significant differences in its surface chemical composition. IR analysis confirmed this hypothesis by revealing a characteristic band at 1766 cm^{-1}, corresponding to the C═O stretching of carboxylic acid groups, present only on ND^{asrec}_{HPHT} (Figure S2b). This feature is responsible for the negative zeta potential that ensures the colloidal stability. On both types, additional signatures of oxidized terminations, such as alcohols and epoxy groups, are indicated by bands at 1290 and 1090 cm^{-1} corresponding to symmetric and asymmetric C−O stretching modes, respectively. Bands at 3670−2670 and 1620 cm^{-1}, associated with the O−H stretching and bending modes, respectively, are also observable. These may originate from alcohol functions or from adsorbed water on the ND surface. Finally, ND^{asrec}_{DET} shows a structure between 2800 and 2950 cm^{-1} corresponding to aliphatic C−H stretching modes due to hydrogen terminations and/or nondiamond phases on the surface.

Using high-frequency (X-band, 9 GHz) EPR acquisitions, we can assess that both ND_{HPHT} and ND_{DET} (10 mg mL^{-1}) samples contain electron spins with a main spectroscopic splitting factor (g-factor) = g_e = 2.0027 ± 0.0002. Among impurities other than carbon, some paramagnetic and ferromagnetic impurities originating from transition metal ions (Fe^{3+}, Cr^{3+}, Mn^{2+}, Co^{2+}, Ni^{2+}, or Cu^{2+}) can be found in diamond suspensions. HR-TEM energy-dispersive X-ray (EDX) confirmed the presence of Al, Fe, or Zr (Table S1) randomly distributed within the bulk, among other elements, with uniform distribution.[39,44] As a result of the grinding and explosion processes (milling with zirconium oxide micrometer-sized beads; sonic mechanical disintegration of corrosion products from the explosion chamber wall), noncarbon elements were incorporated within the suspension. ICP-AES analysis estimated the bulk composition of ND^{asrec}_{DET} and ND^{asrec}_{HPHT} suspensions. The resulting concentrations normalized per ND suspension are given in Table S2. Among the most notable differences between both samples, one has to mention the high zirconium content detected in the ND_{DET} sample (with around 14 ng per mg ND_{DET} and below the LOD in the ND_{HPHT} sample) as a consequence of its dispersion process (ND_{DET} dispersion is achieved using the zirconia beads-assisted method).

Figure 2 shows the main resonance EPR single lines at 343 mT (extension) for the ND_{HPHT} and ND_{DET} samples, resulting mainly from structural defects (dangling bonds). For small-sized nanodiamonds (<70 nm), it can be assumed as a two-component deconvolution since the EPR line has a larger line width, with a similar signal resonance g-factor mainly attributed to the free electron resonance (g_e = 2.0027) but with different line width contributions:[45] (i) a broad spin-1/2 Lorentzian component assigned to C−C carbon dangling bonds on the particle surface and in the nanoparticle core and (ii) a narrow spin-1/2 Lorentzian component attributed to defects in the diamond lattice.[45] Due to the relatively high local spin densities and their close proximity, a main characteristic of a

https://doi.org/10.1021/acs.langmuir.4c05169
Langmuir XXXX, XXX, XXX−XXX

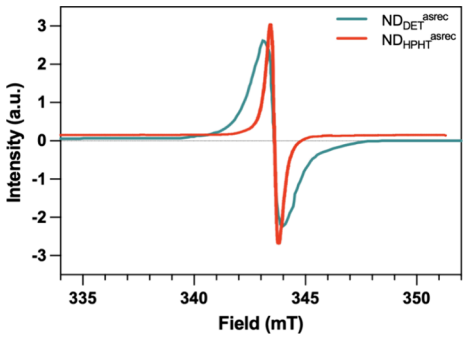

Figure 2. Typical analysis of high-frequency (X-band) EPR profiles of ND_{DET}^{asrec} (green) and ND_{HPHT}^{asrec} (red) suspensions (10 mg mL^{-1}) recorded at room temperature (main resonance signal) around the resonant magnetic field of the signal (g = 2.0027). Microwave frequency: 9 GHz.

nanosized system, these defects are able to mutually interact and, additionally, can interact with nearby P1 centers, increasing the line width. Here, the main differences between nanodiamonds are the production origin, crystallographic core, internal/surface defects, purification, surface chemistry, agglomeration state, presence of sp^2-carbon, and material size. The experimental resonance measured on the ND_{DET}^{asrec} and ND_{HPHT}^{asrec} was characterized by peak-to-peak line widths of 0.96 and 0.38 mT, respectively, at a resonance field B_0 ~343.5 mT. To understand the surface etching modification, nanodiamond source, or size effect, we compared the EPR signal peak-to-peak line width (lwpp). It is worth noting that similar 18 nm-ND^{HPHT} particles from a different provider have been previously reported,[46] with a focus on particles of similar size and characteristics.

Physicochemical Modifications of NDs. *Air Oxidation Process.* ND_{DET} nanodiamonds have a complex surface nature with a higher density of surface defects, amorphous and graphitic carbons, and a wide diversity of functional groups, which can be modulated by surface oxidation to generate acid functions. Oxidation by air annealing provides an efficient method for oxidizing ND surface and removing nondiamond carbon, including paramagnetic radical-like centers (i.e.,

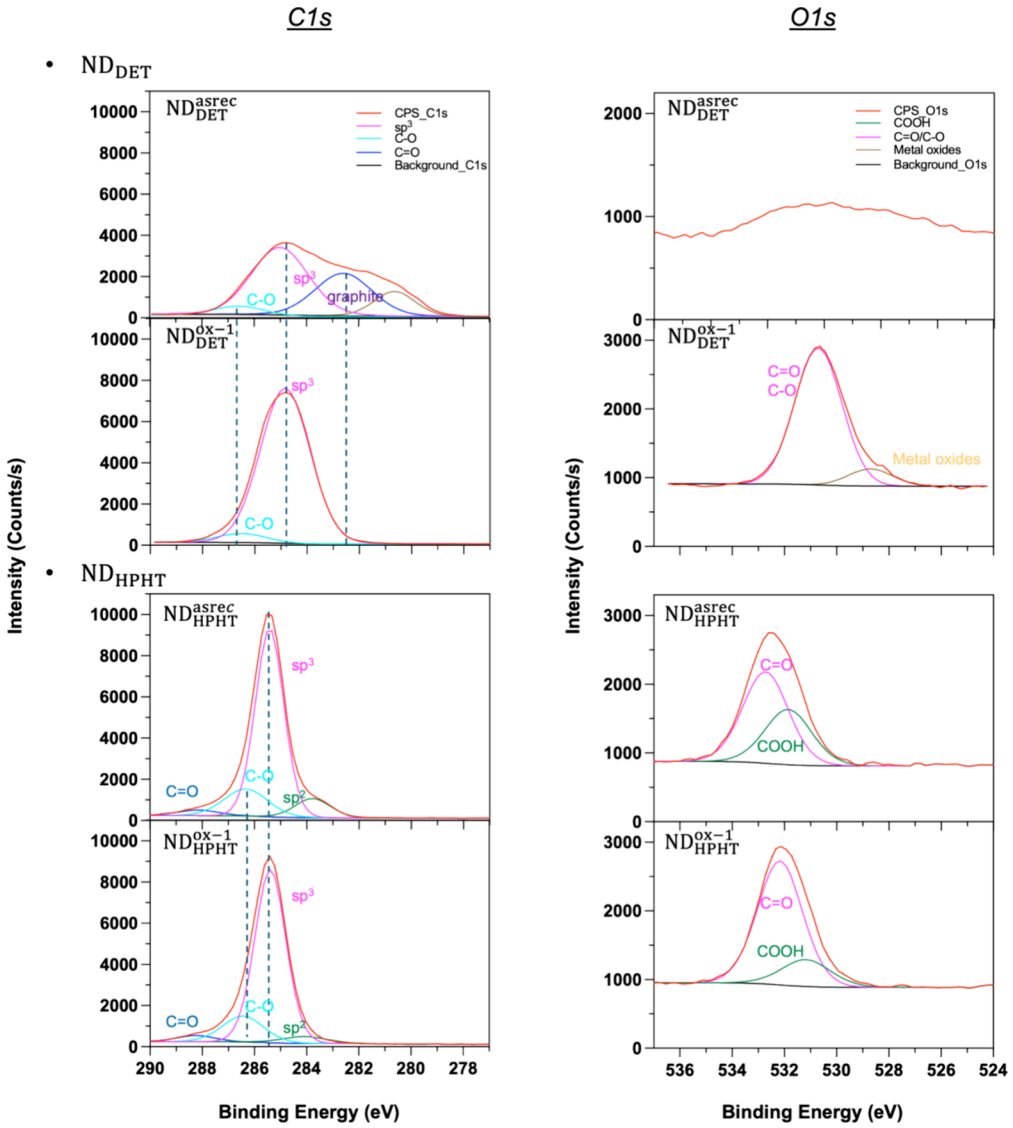

Figure 3. XPS data. Deconvoluted and experimental *C 1s* and *O 1s* fits of ND_{DET} and ND_{HPHT} (columns) obtained before and after air annealing for 4 h. Highlighted *C 1s* and *O 1s* data can be found in Table S3.

https://doi.org/10.1021/acs.langmuir.4c05169
Langmuir XXXX, XXX, XXX−XXX

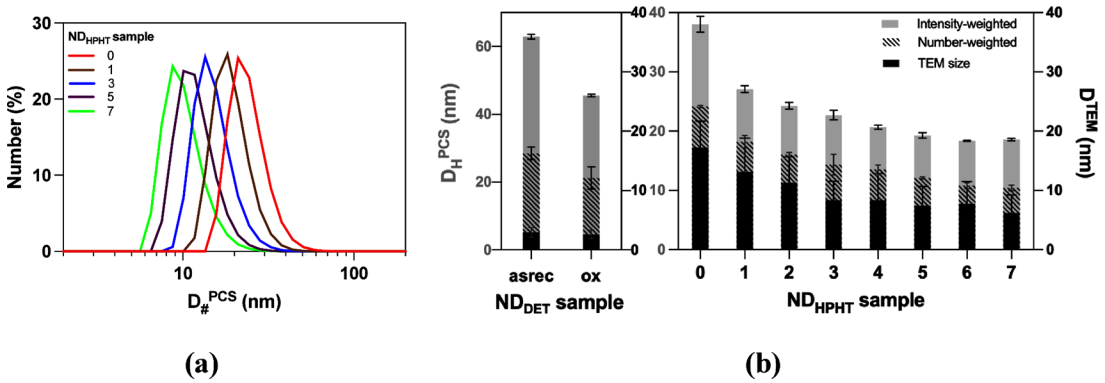

Figure 4. Size distributions. (a) Number size distributions obtained by size exclusion, starting from raw ND_{HPHT}^{asrec}. Only ND_{HPHT} fragments isolated after one, three, five, and seven cycles (16,800*g*) of 60 min increment are shown for clarity. (b) Size distribution histograms by intensity- and number-weighted distributions and TEM sizes ± standard deviations plotted as a function of the number of cycles (ND_{HPHT}^{asrec} is written as "0", ND_{HPHT}^{1} referred to as "1", etc.) and comparison to ND_{DET} colloids. Note that the *y* axis ($D_{\#}^{PCS}$) for ND_{DET} and ND_{HPHT} samples is adjusted between nanodiamond sample types for clarity.

dangling bonds).[34] Prior to this, thermogravimetric analyses (TGAs) were performed on these materials to evaluate their thermal behavior applying a heating rate of 10 °C/min (Figure S1a); ND_{DET} and ND_{HPHT} begin to decompose at 515 and 483 °C, respectively, with a weight loss of 5%. A weight loss of 50% is observed between 546 and 560 °C. Based on the information resulting from TGA analysis, air-annealing conditions at 400 °C (ox-1), 450 °C (ox-2), 480 °C (ox-3), or 550 °C (ox-4) for 4 h were applied to evaluate the impact of oxidation on NDs' physicochemical properties, especially with regard to their surface chemical composition, graphitization, or dangling bonds onto the ND surface. Thanks to the annealing process, the weight decreases to 96 and 87% at 400 °C, 90 and 86% at 450 °C, 84 and 68% at 480 °C, and 31 and 1% at 550 °C after 4 h of air annealing for ND_{HPHT} and ND_{DET}, respectively (Figure S2).

In ND_{DET} samples, primary particles appear as tightly bounded clusters forming large aggregates in the suspension as a result of their surface nature due to various functional groups (i.e., ether, epoxide, hydroxyl, carbonyl, and carboxyl). The first observation is that the applied treatments improve the dispersion as well as the colloidal stability by preventing NDs from aggregation. This observation is confirmed by PCS analyses. While no significant difference in the core size was noted by TEM (5.2 ± 1.4 vs 4.5 ± 1.2 nm), PCS indicates that this treatment has a considerable decrease in the mean hydrodynamic size from 63 nm ($D_{\#}^{PCS}$ = 28 nm) for ND_{DET}^{asrec} to 45−48 nm ($D_{\#}^{PCS}$ = 15−22 nm) for oxidized ND_{DET} samples, respectively. The evolution of the zeta potential in relation to pH changes indicates a shift from positive to negative values (from ζ = +46 to −44 mV after oxidation at pH 7.3; Figure S3), suggesting an increase of colloidal stability through ionic repulsion. Indeed, FTIR analysis reveals the emergence of a carbonyl C═O stretching band around 1780 cm^{-1}, indicating the formation of carboxylic groups on the surface. This is responsible for the negative zeta potential, in concomitance with the disappearance of C−H stretching modes that were previously observed. Figure S4 also shows that the annealing at 400 °C leads to a spectrum similar to those obtained under other conditions (up to 500 °C). In accordance with FTIR, XPS data (Figure S5) showed an increase in the total oxygen content in the $ND_{DET}^{ox\text{-}1}$ sample after air annealing (Table S3); their atomic concentrations were calculated from the corresponding *C 1s* and *O 1s* core-level peak intensities (286−280 and 531−528 eV, respectively). The main difference in elemental composition in relative percentage terms is expressed by the *O 1s/C 1s* ratio. While ND_{DET}^{asrec} nanodiamonds contain 3.80% oxygen and 94.20% carbon (the remaining 2% consists of nitrogen) (*O 1s/C 1s* = 0.04), $ND_{DET}^{ox\text{-}1}$ nanodiamonds contain 9.41% oxygen and 89.19% carbon (*O 1s/C 1s* = 0.10). This corresponds to a 59% increase in oxygen and a 5% reduction in carbon after air annealing under ox-1 conditions. Following the air-annealing treatment, the surface composition of ND_{HPHT} seems to be less affected as suggested by the slight evolution observed in the various FTIR spectra (Figure S4). This observation suggests that, unlike ND_{DET}^{asrec}, the ND_{HPHT}^{asrec} surface was already completely oxidized due to the grinding process nature.[47] XPS (Figure 3) confirms those observations with no significant difference observed for ND_{HPHT} samples under the same air-annealing procedure (*O 1s/C 1s* = 0.11). After their US-assisted dispersion in DI water, PCS measurements indicate that controlled air annealing at 400, 450, 480, or 550 °C for 4 h compared to the ND_{HPHT}^{asrec} procedure has no influence on their colloidal behavior based on their hydrodynamic particle size distribution profiles (around D_{H}^{PCS} 36 nm) and zeta potential values (around ζ = −45 mV at pH 7.4). Overall, the quantitative analysis of the evolution of the carboxylic acid content in ND_{DET} samples indicated an increase of 19 to 27 nmol mg^{-1} between ND_{DET}^{asrec} and $ND_{DET}^{ox\text{-}1}$ conditions as determined by Boehm conductometric titration. In the case of ND_{HPHT}, no significant difference was noticed in these conditions (32 nmol mg^{-1}). This average amount corresponds to 0.36 COOH groups per nm^2 of the spherical $ND_{DET}^{ox\text{-}1}$ particle surface.

Size Exclusion Process. Due to the polydispersity of ND_{HPHT}, we use a simple size exclusion approach to reduce the particle size distribution and approximate the distribution obtained for ND_{DET} after thermal treatment. The size sorting process using centrifugation is a common and simple approach to satisfying colloid fractionation.[35,36] Previous reports showed that MSY 0-0.05 (25 nm median size) is composed of 59% (based on number-weight distribution) of NPs smaller than 17 nm, in particular, 33% of 5 nm ND_{HPHT}, as revealed by TEM analysis.[36] Herein, the high polydispersity (1.79) of the ND_{HPHT}^{asrec} material offers the obvious advantage of being able to be separable into distinct subdivision fractions starting from the crude ND_{HPHT}^{asrec} ($0.5\%_{wt/v}$). We assumed a similar distribution in the MSY 0-0.03 sample. To roughly evaluate

https://doi.org/10.1021/acs.langmuir.4c05169
Langmuir XXXX, XXX, XXX−XXX

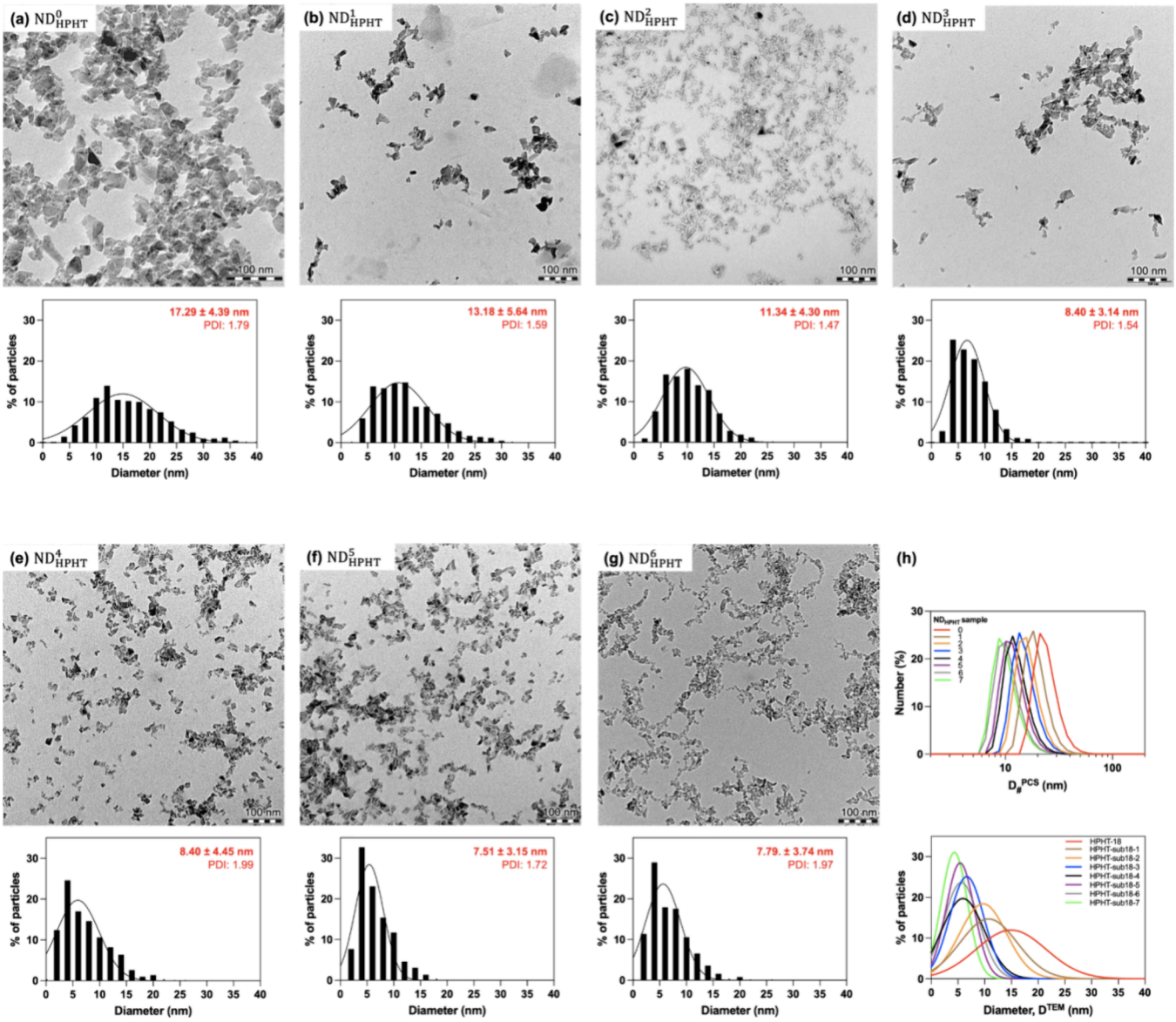

Figure 5. Size measurements on ND_{HPHT} size exclusion particles. TEM images (a−g) (scale bars: 100 nm) and statistical analysis after centrifugation with 60 min of increment starting from the ND_{HPHT}^{asrec} sample (core size approximately 18 nm). The histogram diameter axis is set by a 2 nm increment for clarity. (h) Dynamic size distributions (number-weighted distributions) of the isolated $ND_{HPHT}^{sub\text{-}17}$ fractions following centrifugation treatment at 16,800*g* starting from ND_{HPHT}^{asrec} (0 min), showing a shift toward smaller $D_{\#}^{PCS}$ distributions (up). Comparison of TEM size distributions using histograms fitted with a log-normal function (down).

the size distribution influenced by centrifugation, we employed a constant high speed (16,800*g*) with extended durations in 60 min increments to generate a series of sub-17 nm fractions. After each centrifugation cycle, the supernatant was carefully separated to isolate the ND_{HPHT} sub-17 nm fractions. By following this procedure, we were able to systematically reduce the size of the ND_{HPHT} sample; substantial differences were observed between the recorded distributions, indicating a shift toward smaller particle diameters, as confirmed by PCS measurements (Figure 4). Starting from the initial ND_{HPHT}^{asrec} material ($D_{\#}^{PCS}$: 24.2 nm; PDI: 0.188), the number size profiles clearly show a significant reduction in size distribution well below $D_{\#}^{PCS}$ 13.2 nm (PDI: 0.164) after the first treatment cycle (1 × 60 min; ND_{HPHT}^{1} sample).

Efficient size exclusion was observed from the third centrifugal treatment (ND_{HPHT}^{3} sample; $D_{\#}^{PCS}$: 14.3 nm (PDI: 0.132)). In correlation with DLS, TEM analysis confirmed the PCS observations, showing an evolution of the mean size from 17.3 ± 4.4 nm (PDI: 1.79) to 8.4 ± 3.1 nm (PDI: 1.54) (Figure 5) for raw to ND_{HPHT}^{3} (37% in particle concentration), as depicted in the proposed sorting process. The particle size of sub-17 nm HPHT thus approached that obtained for detonation particles. No significant difference in the size profile could be noticed when comparing ND_{HPHT}^{3} to the other subfractions. Overall, this size treatment effectively isolated the desired sub-17 nm particles, resulting in a relatively monodisperse fraction (Table S4), despite a relatively low yield (around 7.5%$_{wt}$ in particle concentration), based on the initial colloid concentration as obtained gravimetrically (Figure S6, Table S4).

It must be mentioned that the separation of detonation nanoparticles was not a straightforward applicable process; indeed, 16,800*g* speed treatment led to a nonstable suspension due to their aggregation states caused by the complex structure

https://doi.org/10.1021/acs.langmuir.4c05169
Langmuir XXXX, XXX, XXX−XXX

Table 1. Comparison of the Physicochemical Parameters of Nanodiamonds

sample	ζ pH = 7.3 ± 0.1 (mV)	size		EPR (X-band) (g = 2.0027 ± 0.0002)		EPRI
		$D_{\#}^{PCS}$ (nm)	D_{H}^{PCS} (nm)	lwpp (mT)	N_S (spin/g)	R (mm)
ND_{DET}^{asrec}	+42 ± 2	28.4 ± 1.9	62.9 ± 0.7	0.96	6.6×10^{19}	>2
$ND_{DET}^{ox\text{-}1}$	−40 ± 2	21.2 ± 3.2	45.6 ± 0.4	0.88	5.8×10^{19}	>2
ND_{HPHT}^{asrec}	−39 ± 2	24.2 ± 0.2	36.1 ± 0.2	0.38	1.5×10^{19}	0.7
ND_{HPHT}^{1}	−37 ± 2	27.1 ± 0.6	27.1 ± 0.6	0.27	1.4×10^{19}	>0.5
ND_{HPHT}^{3}	−36 ± 1	14.3 ± 1.8	23.9 ± 0.3	0.23	1.3×10^{19}	0.5
ND_{HPHT}^{5}	−44 ± 2	12.2 ± 0.2	19.3 ± 0.4	0.23	1.0×10^{19}	<0.5
ND_{HPHT}^{7}	−44 ± 2	10.4 ± 0.5	18.6 ± 0.2	0.22	9.8×10^{18}	<0.5
$ND_{HPHT}^{ox\text{-}1}$	−43 ± 1	22.6 ± 0.6	35.4 ± 0.1	0.28	1.6×10^{19}	>0.5
$ND_{HPHT}^{ox\text{-}2}$	−46 ± 1	21.2 ± 0.8	34.5 ± 0.2	0.27	9.1×10^{18}	>0.5
$ND_{HPHT}^{ox\text{-}3}$	−46 ± 1	21.0 ± 1.2	37.8 ± 0.1	0.26	6.7×10^{18}	0.5
$ND_{HPHT}^{ox\text{-}4}$	−47 ± 1	15.6 ± 1.1	32.6 ± 0.5	0.24	2.1×10^{18}	<0.5

of the isolated detonation shoot. Photos of as-received and thermally oxidized particles treated for 60 min at 16,800g are shown in Figure S7. This procedure was not applied to the detonation nanodiamonds due to a lack of colloidal stability resulting from their aggregation state. We note that these particles are usually tightly bound into aggregates despite many efforts (milling aggregates with micrometer-sized ceramic beads) to stabilize individual spherical NPs.[48]

EPR Spectroscopic and Imaging Study for Spatial Resolution. *HPHT-Synthesized Nanodiamonds.* Interestingly, a noticeable line width reduction effect can be observed in EPR spectroscopy from 0.38 mT onward as the average particle size decreases through size exclusion. The EPR features (signal width) of this series of HPHT are presented in Table 1. The line width decreased and then reached a plateau from sample ND_{HPHT}^{3} to ND_{HPHT}^{5} (ND_{HPHT}^{3}; N_s = 1.3 × 10^{19} spin/g) for a value of around 0.23 mT, corresponding to a decrease in the broad component of nearly 40%, for which the ND_{HPHT}^{3} sample appeared as an efficient sample for EPRI investigation (achievable resolution <0.5 nm). This set of size variations in ND_{HPHT} resulted in a weak decrease of spins per gram (N_S) but, strikingly, an efficient decrease in the broad component of the signal. The comparison of the physicochemical parameters collected for the different series of nanodiamonds is summarized in Table 1.

Alternatively, thermal annealing of ND_{HPHT} resulted in a decrease in the broad component of the signal. In contrast to detonation nanodiamonds, the air-annealing process has a minimal impact on the spins located on the outer surface due to the surface nature of HPHT particles.

Although FTIR spectroscopy did not reveal any significant qualitative differences between the samples after thermal treatments, there was a significant impact on their lwpp. Raman spectroscopy was used to determine these differences. This technique provided additional information about their structural changes. The Raman spectrum of ND_{HPHT} is shown in Figure S8a and displays the following characteristics:[49] (i) a peak at 1330 cm^{-1} (dotted line) associated with the first-order diamond peak (C*, diamond phase); (ii) a deconvoluted peak at 1350 cm^{-1} assigned to sp^2-hybridized bond deformation mode (D-band); (iii) 1470 cm^{-1} that could be attributed to the presence of nitrogen-vacancy defects in the diamond lattice; (iv) a broad component at 1570−1590 cm^{-1} due to allotropic forms of carbon sp^2-graphitic carbon covering the diamond core (G-band); and (v) a band at 1685 cm^{-1} characteristic of C−OH/C═O bending vibrations at the particle surface. In addition to the above-mentioned peaks, the ND_{HPHT} 1580 cm^{-1} peak (G-band) decreases due to the air-annealing progress of HPHT samples (400 to 550 °C) among the other nondiamonds' absorption (Figure S8a). Indeed, Raman spectra of HPHT particles show a considerable increase in the diamond peak (C*) intensity compared to the broad sp^2-related band (1500−1800 cm^{-1}) of the air-annealed samples, and its shift 1332−1333 cm^{-1} becomes dominant (Figure S8b). It is evident that the air-annealing of the HPHT powder at 550 °C for 4 h ($ND_{HPHT}^{ox\text{-}4}$) considerably reduces the graphitic content as the G-band is further suppressed.

For both strategies, these distinct treatments enabled adequate control of the size and surface area, leading to the fine-tuning of parameters and lower N_S content. Overall, the EPR signal of HPHT particles typically exhibits a narrower line width for the narrow component compared to other types of nanodiamonds. This suggests a higher degree of order in the material, although line widths are also influenced by other factors, such as the initial content of P1 centers and exchange interactions between spins within the particle.[45] This is particularly true as the size decreases from micrometers (100 μm) to nanometers (20 nm) as reported in the literature.[50] Distinctive modifications (including signal line width) have appeared in the EPR spectrum when the average size of particles in polydisperse samples decreases.[50]

DET Nanodiamonds. In contrast, the EPR signal of detonation nanodiamonds typically exhibits a broad line width (lwpp = 0.96 mT) due to the presence of multiple paramagnetic defects such as structural defects, dangling bonds, impurities, and graphite and diamond allotropes.[51] Overall, HPHT nanodiamonds exhibit a narrower signal than ND_{DET}^{asrec}, representing a reduction of almost 60% of the fwhm (full width at half-maximum). In addition, the concentration of RPC (spin S = 1/2) was estimated to be N_s = 1.5 × 10^{19} spin/g on the HPHT colloid, which is ∼4.4 times less than the detonation sample (N_s = 6.6 × 10^{19} spin/g). Assuming that ND_{DET}^{asrec} particles are spherical, an experimental value of approximately 5 RPC/particle is obtained, and the spins are inhomogeneously distributed according to the literature.[48,51] Interestingly, we observe a reduction in the EPR signal line width resulting from the decrease in spin density at the particle surface during air-oxidation treatment. For comparison, oxidative treatment of ND_{DET} reduces the broad component by 10%, associated with impurities near the particle surface (mainly dangling bonds) for the ox-1 sample. This fact illustrates the importance of surface properties and sets for surface development.

https://doi.org/10.1021/acs.langmuir.4c05169
Langmuir XXXX, XXX, XXX−XXX

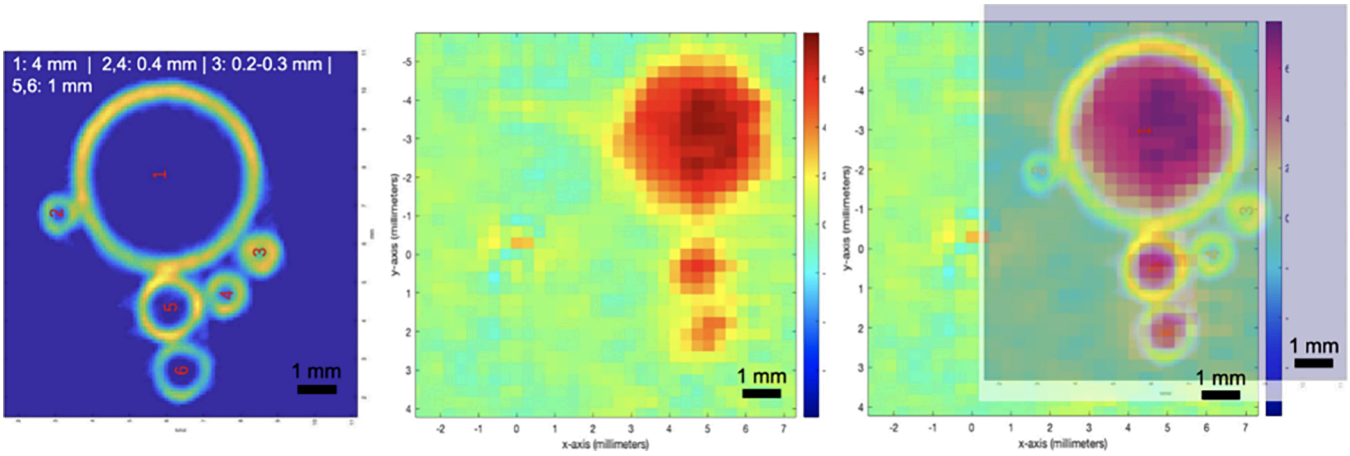

Figure 6. L-band EPR imaging experiment of the ND^{asrec}_{HPHT} sample. Anatomic micro-CT image (left), corresponding 2D image (ZY) of glass capillaries containing ND suspensions imaged by EPRI (middle), and the superimposed spatial registration of the EPR image to the corresponding micro-CT scan (right). EPRI parameters: experimental time: 71 min; lwpp: 0.35 mT; and FOV: 37.55 mm.

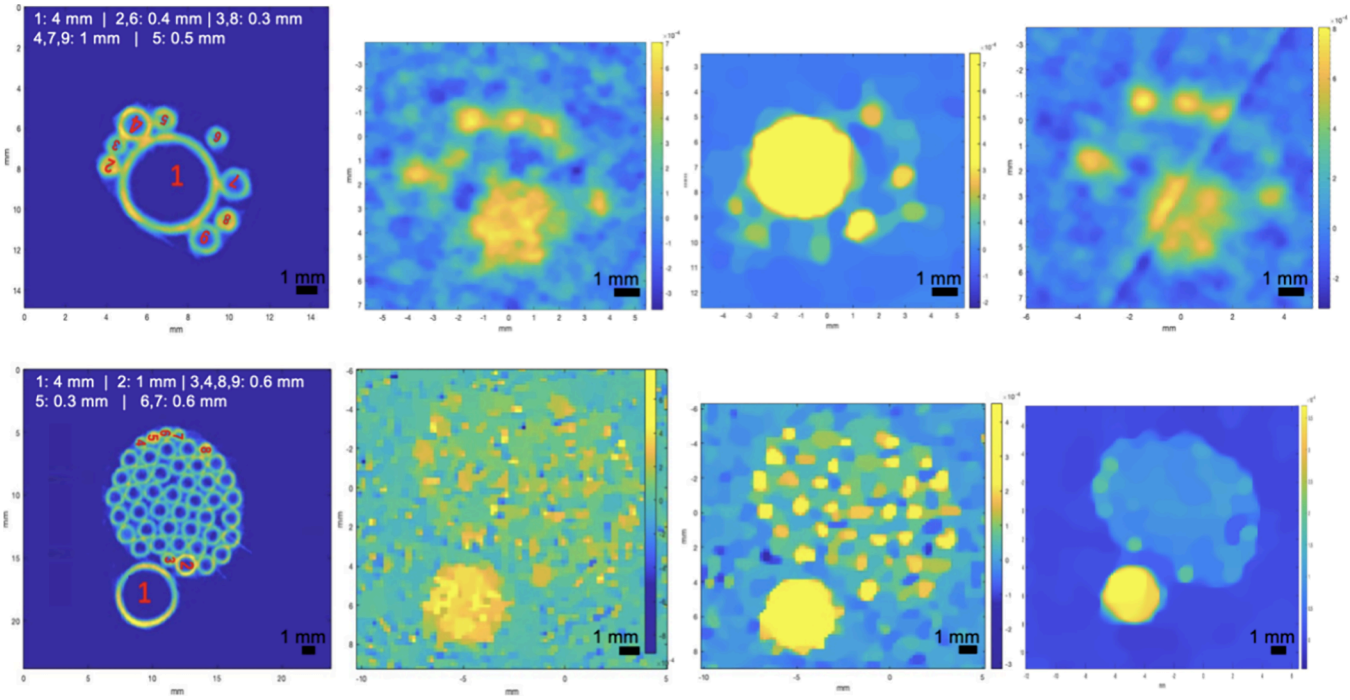

Figure 7. L-band EPR images of the ND^{3}_{HPHT} sample. EPRI and the phantom object anatomic CT-microtomography (left) and 2D images (ZY) of glass capillaries containing aqueous suspensions of NDs from left to right according to iteration number, regularity parameter λ'. ND densities of 10 mg mL^{-1} (up) and 20 mg mL^{-1} (down) were imaged.

The main advantage of ND_{HPHT} over ND_{DET} is the uniform crystallinity and purity with a relatively low and localized concentration of spin-resonant lattice defects. This is crucial for their spectroscopic characteristics and imaging applications, as they can stably host narrow single-line EPR components. The concentration of radical-like paramagnetic centers, including impurities and dangling bonds, can be well-suited to EPRI applications with significant decreases in peak-to-peak derived line width after ND_{HPHT} size exclusion. Three centrifugation cycles of the ND_{HPHT} nanodiamonds yield promising EPR features (minimal lwpp obtained = 0.22 mT). In an interesting feature involving nanodiamonds, we highlight how the use of NDs can be relevant to afford a unique EPR contrast signature through long-term stable paramagnetic centers.

L-Band EPR Imaging Study for Spatial Resolution. Imaging capabilities of NDs have been further evaluated in L-band (1 GHz) EPR spectroscopy (Figure S9) and imaging for low-field frequency measurements. EPR images are recorded similarly to a conventional EPR spectrum, with magnetic field gradients applied in a range of different orientations around the sample (gradient = 4 mT/cm). The achievable resolution in an EPRI experiment is based on concepts similar to those of MRI acquisition. Formally, a common definition of resolution is the determination of the number of pixels in a specified field of view (FOV). In this case, the theoretical spatial resolution in EPRI is closely proportional to the peak-to-peak line width of the EPR spectroscopic absorption curve (lwpp) and the inverse of the gradient intensity (∇); typically, R = lwpp/∇. Overall, a narrower line width and stronger gradients allow for

https://doi.org/10.1021/acs.langmuir.4c05169
Langmuir XXXX, XXX, XXX−XXX

high-resolution EPR images ($\lim_{\nabla \to \infty} R = 0$), which are limited by the magnetic field produced by the gradients[52] for small gradient strength (∇ < 10% principal magnetic field). Two-dimensional imaging also implies spatial resolution represented by the pixel resolution (R_{Pixel}= FOV/number of pixel) of the imaging system with correct image reconstruction.[41] However, broad peak-to-peak line widths can limit the application of various types of NPs for resolution enhanced imaging, which tends to give special attention to nanometric ND_{HPHT}. In this case, by employing a deconvolution process to recover a spatially homogeneous spin density distribution, spatial resolutions of less than 0.7 mm could be obtained in the improved EPR imaging system starting from the raw ND^{asrec}_{HPHT} sample. Using mathematical algorithms and imaging optimizations, we present promising preliminary EPRI acquisitions of capillary phantoms after image reconstruction. The experimental resolution of ND^{asrec}_{HPHT} was evaluated by image analysis based on quartz capillaries containing mean 18 nm size monocrystalline particles with inner-diameter sizes of 0.2, 0.3, 0.4, 0.5, 0.6, 1, and 4.0 mm. Imaging of raw ND^{asrec}_{HPHT} (lwpp = 0.38 mT; RPC = 0.442 mM) filled into capillaries at a similar concentration (10 mg mL^{-1}) showed a strong detectable signal. An achievable resolution of <0.7 mm was observed on Figure 6 with spatial registration and fusion of raw EPRI and X-ray micro-CT on the same object. In contrast, ND_{DET} (lwpp = 0.98 mT) did not provide the expected resolution since R > 2 mm under the data acquisitions (R = 0.23 mm for a FOV of 32 mm) (data not shown). We can mention that the ND_{DET} EPR signal operating at microwave frequency of 1 GHz presents a known spectral resolution limitation compared to the ND_{HPHT} sample. Despite a 4.4-fold decrease in RPC content compared with ND_{DET}, typically exhibiting a spin density N_S of 6.6×10^{19} vs 1.5×10^{19} spin/g for ND^{asrec}_{DET} and ND^{asrec}_{HPHT}, respectively, the latter still demonstrates good sensitivity and threshold detection.

Additionally, as previously mentioned, the spatial resolution of EPR images (R) depends on probe line widths and the magnetic field strength. Thus, reducing the line width of the sample may enhance image contrast. From all the samples under study, we consider the ND^{3}_{HPHT} colloid to be the most promising (lwpp = 0.23 mT). Furthermore, if the number of spins in a pixel or voxel falls below the detection threshold (<0.4 mm), no image can be acquired under these conditions. On this basis, we investigate the nanodiamond density of the ND^{3}_{HPHT} sample by studying a 10 mg mL^{-1} (RPC = 0.221 mM) (Figure 7; upper line) or 20 mg mL^{-1} (RPC = 0.442 mM) (Figure 7; lower line) suspension. Full details specific to sampling imaging parameters can be found in the paper from Abergel et al.[42] Images were processed according to the number of iterations.

The images above represent the first combined EPRI and micro-CT images offering good resolution of a phantom (R < 0.5 mm) and open the way to the utilization of NDs in the field of EPR imaging.

■ CONCLUSIONS

This study explores the physicochemical properties of nanodiamonds, focusing on size and surface treatments using commercial materials obtained by grinding or detonation synthesis. The difference in production conditions allows one to differ the chemical composition of impurities and their distribution along the crystal as well as control over a predetermined nanoparticle size and shape. Using size exclusion on a polydisperse HPHT sample (mean size 18 nm), a particle size distribution similar to that of detonation nanodiamonds was achieved with improved structural quality and surface uniformity. In addition, we describe thermal oxidation because it is a straightforward approach that allows surface chemistry uniformization leading to oxygen-terminated particles and comparison of EPR features. Furthermore, EPR spectroscopy revealed the promising properties of HPHT nanodiamonds for probing at smaller sizes, demonstrating the capabilities of low-field (1 GHz) EPR imaging. Overall, this study highlights the unique EPR properties of nanodiamonds, specifically the ND^{3}_{HPHT} sample (mean size of 8 nm), and offers prospects for applications in nanomedicine and materials science.

■ ASSOCIATED CONTENT

Supporting Information

The Supporting Information is available free of charge at https://pubs.acs.org/doi/10.1021/acs.langmuir.4c05169.

HRTEM-EDX data (Table S1), ICP data (Table S2), XPS data (Table S3), size data (Table S4), surface analysis (Figure S1), gravimetric measurement (Figure S2), zeta potential data (Figure S3), IR (Figure S4), XPS spectra (Figure S4), size obtained by size exclusion (Figure S6), photographs of ND suspensions through size exclusion process (Figure S7), Raman spectra (Figure S8), and L-band EPR spectrum of ND sample (Figure S9) (PDF)

■ AUTHOR INFORMATION

Corresponding Author

Sophie Laurent − *NMR and Molecular Imaging Laboratory, General, Organic and Biomedical Chemistry Unit, University of Mons, Mons B-7000, Belgium; Center for Microscopy and Molecular Imaging (CMMI), Gosselies B-6041, Belgium;* Phone: +32-65373594; Email: sophie.laurent@umons.ac.be

Authors

Sarah Garifo − *NMR and Molecular Imaging Laboratory, General, Organic and Biomedical Chemistry Unit, University of Mons, Mons B-7000, Belgium;* orcid.org/0000-0003-1137-7690

Dimitri Stanicki − *NMR and Molecular Imaging Laboratory, General, Organic and Biomedical Chemistry Unit, University of Mons, Mons B-7000, Belgium*

Thomas Vangijzegem − *NMR and Molecular Imaging Laboratory, General, Organic and Biomedical Chemistry Unit, University of Mons, Mons B-7000, Belgium*

Philippe Mellet − *University of Bordeaux, CNRS, CRMSB, UMR 5536, Bordeaux F-33000, France; INSERM, Bordeaux F-33000, France;* orcid.org/0000-0001-5499-9735

Hugues A. Girard − *Université Paris-Saclay, CEA, CNRS, NIMBE, Gif sur Yvette 91191, France*

Jean-Charles Arnault − *Université Paris-Saclay, CEA, CNRS, NIMBE, Gif sur Yvette 91191, France;* orcid.org/0000-0002-1081-3449

Sylvie Bégin-Colin − *UMR CNRS-UdS 7504, Institut de Physique et Chimie des Matériaux, CNRS, University of*

Strasbourg, Strasbourg 67034, France; orcid.org/0000-0002-2293-2226

Yves-Michel Frapart − *University of Paris Cité, CNRS, LCBPT, Paris F-75006, France*

Robert N. Muller − *NMR and Molecular Imaging Laboratory, General, Organic and Biomedical Chemistry Unit, University of Mons, Mons B-7000, Belgium; Center for Microscopy and Molecular Imaging (CMMI), Gosselies B-6041, Belgium*

Complete contact information is available at: https://pubs.acs.org/10.1021/acs.langmuir.4c05169

Notes

The authors declare no competing financial interest.

■ ACKNOWLEDGMENTS

The authors acknowledge P. Massot from CNRS-UMR5536 and R. Abregel from MAP5-UMR 8145 for their invaluable assistance throughout the project. The authors thank the laboratories of J.-M. Raquez for providing access to TGA equipment, P. Duez for the access to ICP-AES instrument, and the Center for Microscopy and Molecular Imaging (CMMI, supported by the European Regional Development Fund and the Walloon Region). The authors are also grateful to Materia Nova for the collaboration and support in the XPS characterizations. This work was supported by the Fond National de la Recherche Scientifique (FNRS), the ARC Programs of the French Community of Belgium, and the Walloon Region (Prother-Wal and Interreg projects).

■ REFERENCES

(1) Danhier, P.; Gallez, B. Electron Paramagnetic Resonance: A Powerful Tool to Support Magnetic Resonance Imaging Research. *Contrast Media Mol. Imaging* **2015**, *10* (4), 266−281.

(2) Kempe, S.; Metz, H.; Mäder, K. Application of Electron Paramagnetic Resonance (EPR) Spectroscopy and Imaging in Drug Delivery Research − Chances and Challenges. *Eur. J. Pharm. Biopharm.* **2010**, *74* (1), 55−66.

(3) Abbas, K.; Babić, N.; Peyrot, F. Use of Spin Traps to Detect Superoxide Production in Living Cells by Electron Paramagnetic Resonance (EPR) Spectroscopy. *Methods* **2016**, *109*, 31−43.

(4) Bordignon, E. EPR Spectroscopy of Nitroxide Spin Probes. In *eMagRes*; Harris, R. K.; Wasylishen, R. L., Eds.; John Wiley & Sons, Ltd: Chichester, UK, 2017; pp 235−254. .

(5) Tran, D.-N.; Li-Thiao-Te, S.; Frapart, Y.-M. Parameter Estimation for Quantitative EPR Spectroscopy. *IEEE Trans. Instrum. Meas.* **2021**, *70*, 1−7.

(6) Krishna, M. C.; Subramanian, S. The Development of Time-Domain In Vivo EPR Imaging at NCI. *Appl. Magn. Reson.* **2021**, *52* (10), 1291−1309.

(7) Sahu, I. D.; Lorigan, G. A. Electron Paramagnetic Resonance as a Tool for Studying Membrane Proteins. *Biomolecules* **2020**, *10* (5), 763.

(8) Hofmann, L.; Ruthstein, S. EPR Spectroscopy Provides New Insights into Complex Biological Reaction Mechanisms. *J. Phys. Chem. B* **2022**, *126* (39), 7486−7494.

(9) Galazzo, L.; Bordignon, E. Electron Paramagnetic Resonance Spectroscopy in Structural-Dynamic Studies of Large Protein Complexes. *Prog. Nucl. Magn. Reson. Spectrosc.* **2023**, *134*−*135*, 1−19.

(10) Passeri, D.; Rinaldi, F.; Ingallina, C.; Carafa, M.; Rossi, M.; Terranova, M. L.; Marianecci, C. Biomedical Applications of Nanodiamonds: An Overview. *J. Nanosci. Nanotechnol.* **2015**, *15* (2), 972−988.

(11) Chauhan, S.; Jain, N.; Nagaich, U. Nanodiamonds with Powerful Ability for Drug Delivery and Biomedical Applications: Recent Updates on in Vivo Study and Patents. *J. Pharm. Anal.* **2020**, *10* (1), 1−12.

(12) Garifo, S.; Stanicki, D.; Ayata, G.; Muller, R. N.; Laurent, S. Nanodiamonds as Nanomaterial for Biomedical Field. *Front. Mater. Sci.* **2021**, *15* (3), 334−351.

(13) Pichot, V.; Muller, O.; Seve, A.; Yvon, A.; Merlat, L.; Spitzer, D. Optical Properties of Functionalized Nanodiamonds. *Sci. Rep.* **2017**, *7* (1), 14086.

(14) Ekimov, E. A.; Shiryaev, A. A.; Grigoriev, Y.; Averin, A.; Shagieva, E.; Stehlik, S.; Kondrin, M. V. Size-Dependent Thermal Stability and Optical Properties of Ultra-Small Nanodiamonds Synthesized under High Pressure. *Nanomater.* **2022**, *12* (3), 351.

(15) Turcheniuk, K.; Mochalin, V. N. Biomedical Applications of Nanodiamond (Review). *Nanotechnol.* **2017**, *28* (25), 252001.

(16) Ansari, S. A.; Satar, R.; Jafri, M. A.; Rasool, M.; Ahmad, W.; Kashif Zaidi, S. Role of Nanodiamonds in Drug Delivery and Stem Cell Therapy. *Iran. J. Biotechnol.* **2016**, *14* (3), 130−141.

(17) Krok, E.; Balakin, S.; Jung, J.; Gross, F.; Opitz, J.; Cuniberti, G. Modification of Titanium Implants Using Biofunctional Nanodiamonds for Enhanced Antimicrobial Properties. *Nanotechnol.* **2020**, *31* (20), 205603.

(18) Singh, D.; Ray, S. A Short Appraisal of Nanodiamonds in Drug Delivery and Targeting: Recent Advancements. *Front. Nanotechnol.* **2023**, *5*, 1259648.

(19) Wu, Y.; Alam, M. N. A.; Balasubramanian, P.; Ermakova, A.; Fischer, S.; Barth, H.; Wagner, M.; Raabe, M.; Jelezko, F.; Weil, T. Nanodiamond Theranostic for Light-Controlled Intracellular Heating and Nanoscale Temperature Sensing. *Nano Lett.* **2021**, *21* (9), 3780−3788.

(20) Panich, A. M.; Salti, M.; Goren, S. D.; Yudina, E. B.; Aleksenskii, A. E.; Vul, A. Y.; Shames, A. I. Gd(III)-Grafted Detonation Nanodiamonds for MRI Contrast Enhancement. *J. Phys. Chem. C* **2019**, *123* (4), 2627−2631.

(21) Panich, A. M.; Salti, M.; Prager, O.; Swissa, E.; Kulvelis, Y. V.; Yudina, E. B.; Aleksenskii, A. E.; Goren, S. D.; Vul, A. Ya.; Shames, A. I. PVP-coated Gd-grafted Nanodiamonds as a Novel and Potentially Safer Contrast Agent for in Vivo MRI. *Magn. Reson. Med.* **2021**, *86* (2), 935−942.

(22) Kunuku, S.; Lin, B.-R.; Chen, C.-H.; Chang, C.-H.; Chen, T.-Y.; Hsiao, T.-Y.; Yu, H.-K.; Chang, Y.-J.; Liao, L.-C.; Chen, F.-H.; Bogdanowicz, R.; Niu, H. Nanodiamonds Doped with Manganese for Applications in Magnetic Resonance Imaging. *ACS Omega* **2023**, *8* (4), 4398−4409.

(23) Panich, A. M.; Shames, A. I.; Aleksenskii, A. E.; Yudina, E. B.; Vul, A. Y. Manganese-Grafted Detonation Nanodiamond, a Novel Potential MRI Contrast Agent. *Diamond Relat. Mater.* **2021**, *119*, No. 108590.

(24) Panich, A. M.; Salti, M.; Aleksenskii, A. E.; Kulvelis, Y. V.; Chizhikova, A.; Vul, A. Ya.; Shames, A. I. Suspensions of Manganese-Grafted Nanodiamonds: Preparation, NMR, and MRI Study. *Diam. Relat. Mater.* **2023**, *131*, No. 109591.

(25) Garifo, S.; Vangijzegem, T.; Stanicki, D.; Laurent, S. A Review on the Design of Carbon-Based Nanomaterials as MRI Contrast Agents. *Mol.* **2024**, *29* (7), 1639.

(26) Waddington, D. E. J.; Boele, T.; Rej, E.; McCamey, D. R.; King, N. J. C.; Gaebel, T.; Reilly, D. J. Phase-Encoded Hyperpolarized Nanodiamond for Magnetic Resonance Imaging. *Sci. Rep.* **2019**, *9* (1), 5950.

(27) Waddington, D. E. J.; Sarracanie, M.; Zhang, H.; Salameh, N.; Glenn, D. R.; Rej, E.; Gaebel, T.; Boele, T.; Walsworth, R. L.; Reilly, D. J.; Rosen, M. S. Nanodiamond-Enhanced MRI via in Situ Hyperpolarization. *Nat. Commun.* **2017**, *8* (1), 15118.

(28) Ajoy, A.; Nazaryan, R.; Druga, E.; Liu, K.; Aguilar, A.; Han, B.; Gierth, M.; Oon, J. T.; Safvati, B.; Tsang, R.; Walton, J. H.; Suter, D.; Meriles, C. A.; Reimer, J. A.; Pines, A. Room Temperature "*Optical Nanodiamond Hyperpolarizer*": Physics, Design, and Operation. *Rev. Sci. Instrum.* **2020**, *91* (2), No. 023106.

(29) Bobko, A. A.; Kirilyuk, I. A.; Grigor'ev, I. A.; Zweier, J. L.; Khramtsov, V. V. Reversible Reduction of Nitroxides to Hydroxyl-

amines: Roles for Ascorbate and Glutathione. *Free Radic. Biol. Med.* **2007**, *42* (3), 404−412.

(30) Jaymand, M.; Davatgaran Taghipour, Y.; Rezaei, A.; Derakhshankhah, H.; Foad Abazari, M.; Samadian, H.; Hamblin, M. R. Radiolabeled Carbon-Based Nanostructures: New Radiopharmaceuticals for Cancer Therapy? *Coord. Chem. Rev.* **2021**, *440*, No. 213974.

(31) Mochalin, V. N.; Shenderova, O.; Ho, D.; Gogotsi, Y. The Properties and Applications of Nanodiamonds. *Nat. Nanotechnol.* **2012**, *7* (1), 11−23.

(32) Qin, J.-X.; Yang, X.-G.; Lv, C.-F.; Li, Y.-Z.; Liu, K.-K.; Zang, J.-H.; Yang, X.; Dong, L.; Shan, C.-X. Nanodiamonds: Synthesis, Properties, and Applications in Nanomedicine. *Mater. Des.* **2021**, *210*, No. 110091.

(33) Whitlow, J.; Pacelli, S.; Paul, A. Multifunctional Nanodiamonds in Regenerative Medicine: Recent Advances and Future Directions. *JCR* **2017**, *261*, 62−86.

(34) Kovářík, T.; Bělský, P.; Rieger, D.; Ilavsky, J.; Jandová, V.; Maas, M.; Šutta, P.; Pola, M.; Medlín, R. Particle Size Analysis and Characterization of Nanodiamond Dispersions in Water and Dimethylformamide by Various Scattering and Diffraction Methods. *J. Nanopart. Res.* **2020**, *22* (2), 34.

(35) Stehlik, S.; Varga, M.; Ledinsky, M.; Jirasek, V.; Artemenko, A.; Kozak, H.; Ondic, L.; Skakalova, V.; Argentero, G.; Pennycook, T.; Meyer, J. C.; Fejfar, A.; Kromka, A.; Rezek, B. Size and Purity Control of HPHT Nanodiamonds down to 1 Nm. *J. Phys. Chem. C* **2015**, *119* (49), 27708−27720.

(36) Rehor, I.; Cigler, P. Precise Estimation of HPHT Nanodiamond Size Distribution Based on Transmission Electron Microscopy Image Analysis. *Diam. Relat. Mater.* **2014**, *46*, 21−24.

(37) Hannecart, A.; Stanicki, D.; Vander Elst, L.; Muller, R. N.; Brûlet, A.; Sandre, O.; Schatz, C.; Lecommandoux, S.; Laurent, S. Embedding of Superparamagnetic Iron Oxide Nanoparticles into Membranes of Well-Defined Poly(Ethylene Oxide)- *Block* -Poly(ε-Caprolactone) Nanoscale Magnetovesicles as Ultrasensitive MRI Probes of Membrane Bio-Degradation. *J. Mater. Chem. B* **2019**, *7* (30), 4692−4705.

(38) Schmidlin, L.; Pichot, V.; Comet, M.; Josset, S.; Rabu, P.; Spitzer, D. Identification, Quantification and Modification of Detonation Nanodiamond Functional Groups. *Diam. Relat. Mater.* **2012**, *22*, 113−117.

(39) Volkov, D. S.; Proskurnin, M. A.; Korobov, M. V. Elemental Analysis of Nanodiamonds by Inductively-Coupled Plasma Atomic Emission Spectroscopy. *Carbon* **2014**, *74*, 1−13.

(40) Stoll, S.; Schweiger, A. EasySpin, a Comprehensive Software Package for Spectral Simulation and Analysis in EPR. *J. Magn. Reson.* **2006**, *178* (1), 42−55.

(41) Durand, S.; Frapart, Y.-M.; Kerebel, M. Electron Paramagnetic Resonance Image Reconstruction with Total Variation and Curvelets Regularization. *Inverse Probl.* **2017**, *33* (11), 114002.

(42) Abergel, R.; Boussâa, M.; Durand, S.; Frapart, Y.-M. Electron Paramagnetic Resonance Image Reconstruction with Total Variation Regularization. *IPOL* **2023**, *13*, 90−139.

(43) Stehlik, S.; Mermoux, M.; Schummer, B.; Vanek, O.; Kolarova, K.; Stenclova, P.; Vlk, A.; Ledinsky, M.; Pfeifer, R.; Romanyuk, O.; Gordeev, I.; Roussel-Dherbey, F.; Nemeckova, Z.; Henych, J.; Bezdicka, P.; Kromka, A.; Rezek, B. Size Effects on Surface Chemistry and Raman Spectra of Sub-5 Nm Oxidized High-Pressure High-Temperature and Detonation Nanodiamonds. *J. Phys. Chem. C* **2021**, *125* (10), 5647−5669.

(44) Dolmatov, V. Yu.; Lapchuk, N. M.; Lapchuk, T. M.; Nguyen, B. T. T.; Myllymäki, V.; Vehanen, A.; Yakovlev, R. Yu. A Study of Defects and Impurities in Doped Detonation Nanodiamonds by EPR, Raman Scattering, and XRD Methods. *J. Superhard Mater.* **2016**, *38* (4), 219−229.

(45) Shames, A. I.; Zegrya, G. G.; Samosvat, D. M.; Osipov, V. Y.; Vul, A. Y. Size Effect in Electron Paramagnetic Resonance Spectra of Impurity Centers in Diamond Particles. *Phys. E* **2023**, *146*, No. 115523.

(46) Panich, A. M.; Sergeev, N. A.; Shames, A. I.; Osipov, V. Y.; Boudou, J.-P.; Goren, S. D. Size Dependence of ^{13}C Nuclear Spin-Lattice Relaxation in Micro- and Nanodiamonds. *J. Phys.: Condens. Matter.* **2015**, *27* (7), No. 072203.

(47) Petit, T.; Puskar, L. FTIR Spectroscopy of Nanodiamonds: Methods and Interpretation. *Diam. Relat. Mater.* **2018**, *89*, 52−66.

(48) Panich, A. M. Nuclear Magnetic Resonance Studies of Nanodiamonds. *Crit. Rev. Solid State Mater. Sci.* **2012**, *37* (4), 276−303.

(49) Mermoux, M.; Chang, S.; Girard, H. A.; Arnault, J.-C. Raman Spectroscopy Study of Detonation Nanodiamond. *Diam. Relat. Mater.* **2018**, *87*, 248−260.

(50) Zegrya, G. G.; Samosvat, D. M.; Osipov, V. Y.; Vul, A. Y.; Shames, A. I. Size Effect in Electron Paramagnetic Resonance Spectra of Impurity Centers in Diamond Nanoparticles. *Mesoscale Nanoscale Phys.* **2019**, 1−25.

(51) Shames, A. I.; Panich, A. M.; Kempiński, W.; Alexenskii, A. E.; Baidakova, M. V.; Dideikin, A. T.; Osipov, V. Y.; Siklitski, V. I.; Osawa, E.; Ozawa, M.; Vul, A. Y. Defects and Impurities in Nanodiamonds: EPR, NMR and TEM Study. *J. Phys. Chem. Solids* **2002**, *63* (11), 1993−2001.

(52) Bézière, N.; Decroos, C.; Mkhitaryan, K.; Kish, E.; Richard, F.; Bigot-Marchand, S.; Durand, S.; Cloppet, F.; Chauvet, C.; Corvol, M.-T.; Rannou, F.; Xu-Li, Y.; Mansuy, D.; Peyrot, F.; Frapart, Y.-M. First Combined in Vivo X-Ray Tomography and High-Resolution Molecular Electron Paramagnetic Resonance (EPR) Imaging of the Mouse Knee Joint Taking into Account the Disappearance Kinetics of the EPR Probe. *Mol. Imaging* **2012**, *11* (3), 220.

https://doi.org/10.1021/acs.langmuir.4c05169
Langmuir XXXX, XXX, XXX−XXX